IEEE Access
Multidisciplinary | Rapid Review | Open Access Journal

Received November 20, 2017, accepted December 26, 2017, date of publication January 10, 2018,
date of current version February 28, 2018.

Digital Object Identifier 10.1109/ACCESS.2017.2788498

External Force Sensing Based on Cable Tension Changes in Minimally Invasive Surgical Micromanipulators

LINGTAO YU[1], WENJIE WANG[1], AND FENGFENG ZHANG[2]
[1]College of Mechanical and Electrical Engineering, Harbin Engineering University, Harbin 150001, China
[2]School of Mechanical and Electrical Engineering, Soochow University, Suzhou 215021, China

Correspondence author: Wenjie Wang (wangwenjie07@hrbeu.edu.cn)

This work was supported in part by the National Natural Science Foundation of China under Grant 61203358/F0306, in part by the National High Technology Research and Development Program of China under Grant 2015AA043201, in part by the Natural Science Foundation of Heilongjiang Province under Grant F2015034, and in part by the Central University Basic Scientific Research Project under Grant HEUCFM170703.

ABSTRACT Force sensing plays an irreplaceable role in minimally invasive surgery. Effective force sensing leads to more successful operations by preventing secondary damage to the body. Force feedback is a crucial part of any minimally invasive surgical robotic system. Very compact construction and the challenging disinfection method are challenging in regard to building force sensors into the end of micromanipulator. This paper focuses on clamping force sensing and 2-D touch force sensing for a three-degrees-of-freedom cable-driven micromanipulator. The clamping and touch forces can be detected based on the changes in cable tension. A complete dynamic model of the micromanipulator wrist and driving cable is established. A comprehensive resistance neural network model of the system was obtained through comprehensive resistance tests and data fitting. An external force estimation strategy is proposed based on the changes in driving system resistance. The performance and accuracy of the 2-D force and clamping force estimations were verified experimentally; the results show that the force estimation precision is acceptable. The force-sensing technique discussed here may assist in the future to realize micromanipulator force feedback in minimally invasive surgical robots.

INDEX TERMS Force measurement, medical robotics, micromanipulators, surgical instruments.

I. INTRODUCTION

Robot-assisted minimally invasive surgery (RIS) is a popular medical technique across the globe because it provides a better experience for the patient and generally results in favorable postoperative recovery. ZEUS [1] and the Da Vinci [2] are the two most successful minimally invasive surgery robot (MISR) systems. The micromanipulators in these systems are driven by cables. Advancements in robotics technology have helped researchers and developers to resolve many problems inherent to MISR operation, but the lack of force sensing feedback remains problematic [3], [4] as it has an adverse effect on the efficiency and safety of surgery. It is difficult to apply accurate operating force to tissue in performing certain operations as the surgeon cannot directly touch the tissue [5]. Accurate and highly precise force sensing will improve the performance and efficiency of MISR systems by reducing the average peak contact force and contact force, as well as truncating the task execution time.

There has been a wealth of research to date on quantifying tool-tissue interaction force. Existing force sensing methods can be roughly divided into direct detection and indirect detection categories [6]. Direct detection involves installing integrated sensors on the micromanipulators to detect the external force. The strain gauge is the most commonly used force-detecting element. The researcher [7] measured force and tissue characteristics with a strain gauge, for example. The detecting element must be placed far away from the point of interaction force, so the accuracy of force detection is seriously affected by friction. Other researchers [8]–[11] have measured the instrument's force directly by micro-force sensors installed in the manipulator's end. Hammond *et al.* [12] printed strain gauges on a surgical forceps to measure pinch force. The fibre bragg grating also is commonly used. A three-dimensional force detection unit based on fiber bragg grating was explored by Peirs *et al.* [13], Puangmali *et al.* [14], and Lim *et al.* [15]

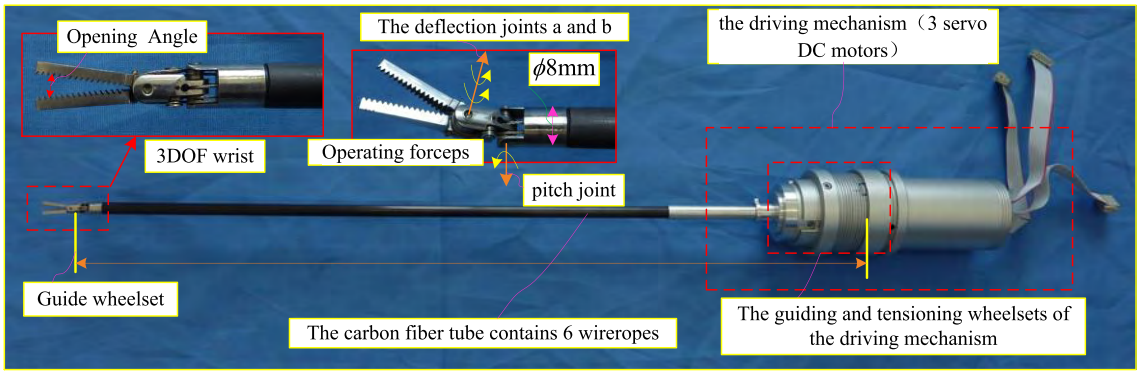

FIGURE 1. Experimental prototype of 3-DOF micromanipulator.

conducted clamping force tests by installing a grating sensor in the forceps of a micromanipulator. Xie *et al.* [16] developed a new contacted 2D force sensor for flexible micro devices based on optical fiber. Conductive polymer materials can also be used to fabricate detecting elements [17]. Gray and Fearing [18] used capacitive sensor arrays to detect force.

The accuracy of direct detection always is high. Building sensors into the surgical tools, unfortunately, is not only highly expensive but makes the tools too bulky to fully function properly. The MISR instrument is too compact in size to accommodate sensors installed in the manipulator's end. Installing sensors also makes the instrument very challenging to disinfect.

Indirect detection, conversely, involves estimating force by using system information instead of a force sensor. One of the simplest ways to detect force is to detect displacement changes in the elastic element. Rosen *et al.* [19], for example, compared position reference inputs and actual positions as a gripper clamped human tissue – clamping force could be automatically detected as position error appeared. Tholey *et al.* [20] realized the indirect measurement of clamping force by detecting motor current. The error is larger due to the mechanical structure, especially when the clamping force is 0.5 N, the detected value is 0.2 N. Zhao and Nelson [21] similarly used motor current to estimate force in a micro device. The estimation precision of the micromanipulator is about 80% and the biggest error is about 0.5N, he claimed the precision is acceptable. Mayer *et al.* [22] estimated the force information of the micro device via neural network method. Li *et al.* [23] conducted force testing based on a disturbance observer in 3-DOF micro instruments, with a minimum resolution of 0.5 N. The accuracy and resolution of these techniques vary considerably.

In summary, the cost of direct force measuring is high and the limitations are obvious. Cost could be reduced while enhancing adaptability by integrating a sensor on the end of a micro device in order to measure cable tension and estimate the external force of the micromanipulator indirectly. This paper focuses on clamping force sensing and 2D touch force sensing for a 3-DOF cable-driven micromanipulator. We propose an external force estimation strategy based on cable tension changes in the driving system.

The remainder of this paper is organized as follows. The micromanipulator and dynamics modeling process are described in Section II. Comprehensive resistance modeling is discussed in Section III. The introduction of the experiment system and comprehensive resistance estimation experiment are shown in Section IV, and 2D touch force and clamping force detection experiments are discussed in Section V. Conclusions are provided in Section VI.

II. MICROMANIPULATOR AND DYNAMIC MODELING

A. INTRODUCTION TO THE MICROMANIPULATOR

The micromanipulator can be considered a subsystem serving as our research object. The experimental prototype of this system is shown in Fig. 1. The micromanipulator is mainly comprised of a wrist with 3-DOF, a cable-guiding wheelset, and a servo motor driving mechanism. The deflection and the opening DOF were realized through integrating a pair of operational forceps. The three joints are separately driven by two-way steel wire ropes. Wrist-driving moments in the system depend on the differences in cable tension – said tension changes as external force acts on the operating forceps. We explored the relationship between the external force and cable tension changes as the key component of the proposed technique.

B. KINEMATIC MODEL OF MICROMANIPULATOR WRIST

A kinematic and dynamic coordinate system diagram of the wrist joints of the micromanipulator is shown in Fig. 2. The micromanipulator only has two DOF (open-close is not strictly a degree of freedom), so F_{ext}^{x} is perpendicular to the pitch joint and deflection joint; it is not possible to estimate F_{ext}^{x}. In other words, it is only possible to estimate 2D force F_{ext}^{y} and F_{ext}^{z}. F_{ext}^{y} is the basis of the clamping force estimation for the micromanipulator.

The forward kinematics model was established based on the DH method [24]. The parameters of the micromanipulator are listed in Table 1. If $x = a$, $\theta_{2x} = \theta_{2a}$, parameters in

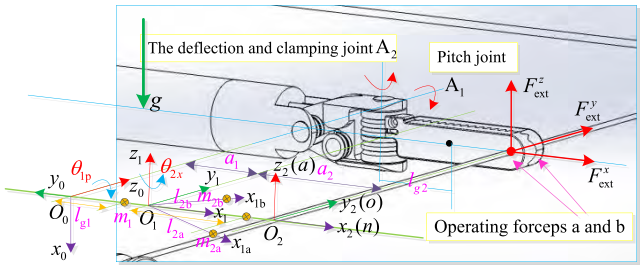

FIGURE 2. Kinematic and dynamic coordinate system diagram of the wrist joints for micromanipulator.

TABLE 1. Link parameters of micromanipulator.

joint	l_i/mm	a_i /rad	d_i/mm	θ_i/rad
1p	$a_1(10)$	$\pi/2$	0	$\theta_{1p}(0)$
2x	$a_2(15)$	0	0	$\theta_{2x}(0)$

Table 1 represent the operating forceps A; if $x = b, \theta_{2x} = \theta_{2b}$, they represent operating forceps B; if $x = c$, $\theta_{2x} = \theta_{2c}$, they indicate that operating forceps A and B move as a whole.

Transformation matrixes between adjacent connecting links (${}^0T_1$ and ${}^0T_{2x}$) can be obtained by the parameters in Table 1, then the forward kinematics model is ${}^0\boldsymbol{T}_{2x} = {}^0T_1\,{}^1T_{2x}$. If the expected position vector of the wrist is $\boldsymbol{p} = \begin{bmatrix} p_X & p_Y & p_Z \end{bmatrix}^{\mathrm{T}}$, the inverse kinematics solution is as shown in (1).

$$\begin{cases} \theta_{1p} = \arccos\left(\dfrac{2a_1p_X}{p_X^2 + p_Y^2 + p_Z^2 + a_1^2 - a_2^2}\right) \\ \theta_{1p} \in [-4\pi/9, 4\pi/9]\,\mathrm{rad} \\ \theta_{2x} = \arccos\left(\dfrac{p_X^2 + p_Y^2 + p_Z^2 - a_1^2 - a_2^2}{2a_1a_2}\right) \\ \theta_{2x} \in [-4\pi/9, 4\pi/9]\,\mathrm{rad} \end{cases} \tag{1}$$

C. DYNAMIC MODEL OF MICROMANIPULATOR WRIST

The micromanipulator wrist has one pitch joint and two deflection joints creating two types of joint combinations. There are two types of corresponding dynamic models: the whole joint dynamics and the separated joint dynamics. The whole joint dynamics synthesize the movement of two operating forceps A and B into their opening angle diagonal movement while synthesizing the mass and the center of mass of the two operating forceps on the diagonal (virtual joint connecting link). The mass of the pitch joint rod is m_1, the mass of the deflection joint rods are m_{2a} and m_{2b}, the opening angle of the operating forceps is θ_3, the arm gravities are l_{g1}, l_{g2a}, and l_{g2b}, the arm gravity can be interpreted as the distance of the center of mass to the joint. The mass of the virtual joints connecting link is m_{2c}, and the distance between the virtual mass and the rotation direction is l_{g2}.

$$\begin{cases} l_{g2} = \dfrac{m_{2a}l_{g2a} + m_{2b}l_{g2b}}{m_{2a} + m_{2b}} \cos(\dfrac{\theta_3}{2}) \\ m_{2c} = m_{2a} + m_{2b} \\ \theta_3 = \theta_{2c} = \dfrac{\theta_{2a} + \theta_{2b}}{2} \end{cases} \tag{2}$$

The kinetic energy K_1 and potential energy P_1 of the pitch joint are:

$$\begin{cases} K_1 = \frac{1}{2}m_1v_1^2 = \dfrac{1}{2}m_1l_{g1}^2\dot{\theta}_{1p}^2 \\ P_1 = -m_1gh_1 = -m_1gl_{g1}\sin(\theta_{1p}) \end{cases} \tag{3}$$

The kinetic energy K_2 and potential energy P_2 of the deflection joint connecting rod are:

$$\begin{cases} K_2 = \frac{1}{2}m_{2x}v_2^2 \\ P_2 = -m_{2x}gh_2 \end{cases} \tag{4}$$

where v_2^2 and h_2 are expressed as follows:

$$\begin{cases} v_2^2 = \left(l_{g2}^2\cos^2(\theta_{2x}) + 2a_1l_{g2}\cos(\theta_{2x}) + a_1^2\right)\dot{\theta}_{1p}^2 \\ \qquad + l_{g2x}\cos^2(\theta_{2x})\dot{\theta}_{2x}^2 \\ h_2 = a_1\cos(\theta_{1p}) + l_{g2x}\cos(\theta_{1p})\cos(\theta_{2x}) \end{cases} \tag{5}$$

The total kinetic energy K and potential energy P of the wrist are:

$$\begin{cases} K = K_1 + K_2 \\ P = P_1 + P_2 \end{cases} \tag{6}$$

The Lagrange function [25] of the dynamics system is $L = K - P$. The dynamics equation is as follows:

$$\boldsymbol{\tau}_x = \boldsymbol{B}(\boldsymbol{q})\ddot{\boldsymbol{q}} + \boldsymbol{C}(\boldsymbol{q}, \dot{\boldsymbol{q}})\dot{\boldsymbol{q}} + \boldsymbol{g}(\boldsymbol{q}) + \boldsymbol{\tau}_{\mathrm{f}}^x + \boldsymbol{J}^{\mathrm{T}}\boldsymbol{F}_{\mathrm{ext}} \tag{7}$$

Where $\boldsymbol{q} = \boldsymbol{\theta} = [\,\theta_{1p}\ \theta_{2x}\,]^{\mathrm{T}}$ is the generalized coordinates of the joints variable, $\boldsymbol{J}^{\mathrm{T}}$ is the force jacobian matrix, $\boldsymbol{F}_{\mathrm{ext}}$ and $\boldsymbol{\tau}_{\mathrm{f}}^x$ are external force and joint friction torque, $\boldsymbol{B}(\boldsymbol{q})\ddot{\boldsymbol{q}}$ is inertia force, $\boldsymbol{C}(\boldsymbol{q}, \dot{\boldsymbol{q}})\dot{\boldsymbol{q}}$ is centrifugal force and coriolis force, and $\boldsymbol{g}(\boldsymbol{q})$ is gravity. The parameters $\boldsymbol{B}(\boldsymbol{q})\ddot{\boldsymbol{q}}$, $\boldsymbol{C}(\boldsymbol{q}, \dot{\boldsymbol{q}})\dot{\boldsymbol{q}}$ and $\boldsymbol{g}(\boldsymbol{q})$ can be determined by the partial derivative and derivative of L. $\boldsymbol{J}^{\mathrm{T}}$ and $\boldsymbol{F}_{\mathrm{ext}}$ are expressed as follows:

$$\begin{cases} \boldsymbol{J}^{\mathrm{T}} = \begin{bmatrix} 0 & 0 & -a_1 - a_2\cos(\theta_{2x}) \\ 0 & a_2 & 0 \end{bmatrix} \\ \boldsymbol{F}_{\mathrm{ext}} = \begin{bmatrix} F_{\mathrm{ext}}^x & F_{\mathrm{ext}}^y & F_{\mathrm{ext}}^z \end{bmatrix}^{\mathrm{T}} \end{cases} \tag{8}$$

If $x = \mathrm{c}$, (7) is the dynamic model of the pitch joint and whole deflection joint. If $x = \mathrm{a}$, (7) is the dynamic model of the pitch joint and deflection joint A. If $x = \mathrm{b}$, (7) is the dynamic model of the pitch joint and deflection joint B.

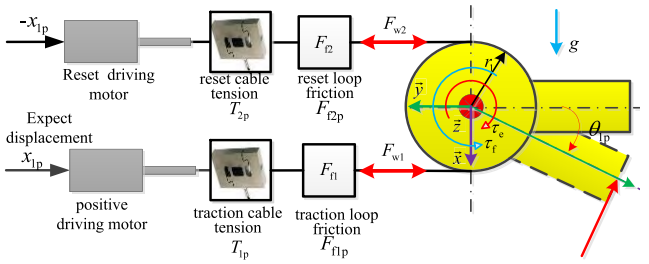

FIGURE 3. Diagram of the pitch joint unit.

D. COMPLETE DYNAMIC MODEL OF THE SYSTEM

There are two types of complete dynamic models for this system. The integrated dynamic model (forceps A and forceps B are regarded as a whole) and the separate dynamic model (forceps A and forceps B are considered separately) are shown in (9) and (10), respectively, where: T_{1p}, T_{2p}, F_{f1p}, F_{f2p}, r_1 are the traction cable tension, reset cable tension, traction loop friction, reset loop friction, and arm of the tension of the pitch joint, respectively as is shown in the figure 3.

This is similar to joint A and joint B. The input torque of the integrated dynamic model is shown in (9), and the input torque of the separate dynamic model is shown in (10):

$$\boldsymbol{\tau}_c = \begin{bmatrix} T_{1p}r_1 \\ T_{1a}r_2 + T_{1b}r_2 \end{bmatrix} - \begin{bmatrix} T_{2p}r_1 \\ T_{2a}r_2 + T_{2b}r_2 \end{bmatrix} - \begin{bmatrix} (F_{f1p} + F_{f2p})r_1 \\ (F_{f1a} + F_{f2a} + F_{f1b} + F_{f2b})r_2 \end{bmatrix} \tag{9}$$

$$\begin{cases} \boldsymbol{\tau}_a = \begin{bmatrix} T_{1p}r_1 \\ T_{1a}r_2 \end{bmatrix} - \begin{bmatrix} T_{2p}r_1 \\ T_{2a}r_2 \end{bmatrix} - \begin{bmatrix} (F_{f1p} + F_{f2p})r_1 \\ (F_{f1a} + F_{f2a})r_2 \end{bmatrix} \\ \boldsymbol{\tau}_b = \begin{bmatrix} T_{1p}r_1 \\ T_{1b}r_2 \end{bmatrix} - \begin{bmatrix} T_{2p}r_1 \\ T_{2b}r_2 \end{bmatrix} - \begin{bmatrix} (F_{f1p} + F_{f2p})r_1 \\ (F_{f1b} + F_{f2b})r_2 \end{bmatrix} \end{cases} \tag{10}$$

When the deflection joint and pitch joint are coupled, it is necessary to compensate for the deflection angle at a value $\theta_{1p}r_1/r_2$, The geometric relationships are shown in (11), where $r_1 = 2$mm, $r_2 = 2.5$mm, x_{1p} and x_{2x} are the displacements of the relative motors.

$$\begin{bmatrix} q_{1p} \\ q_{2x} \end{bmatrix} = \begin{bmatrix} \theta_{1p} \\ \theta_{2x} \end{bmatrix} = \begin{bmatrix} x_{1p}/r_1 \\ (x_{2x} + x_{1p})/r_2 \end{bmatrix} \tag{11}$$

Combining (9), (10) and (7) yield the complete integrated dynamic model and separate dynamic model while regarding the cable tension as input.

III. COMPREHENSIVE RESISTANCE MODELING

A. COMPREHENSIVE RESISTANCE MODELING OF THE PITCH JOINT

The comprehensive resistance model of the pitch joint is established based on the integrated dynamic model (9). The driving force acts on the pitch and the deflection joint is locked. The deflection joint is a continuation of the pitch joint.

$$\begin{bmatrix} \dot{q}_{1p} \\ \dot{q}_{2x} \end{bmatrix} = \begin{bmatrix} \dot{\theta}_{1p} \\ \dot{\theta}_{2x} \end{bmatrix} = \begin{bmatrix} \dot{x}_{1p}/r_1 \\ 0 \end{bmatrix}, \begin{bmatrix} \ddot{q}_{1p} \\ \ddot{q}_{2x} \end{bmatrix} = \begin{bmatrix} \ddot{\theta}_{1p} \\ \ddot{\theta}_{2x} \end{bmatrix} = \begin{bmatrix} \ddot{x}_{1p}/r_1 \\ 0 \end{bmatrix} \tag{12}$$

Combining (7)-(12) yields the dynamic model of the pitch joint:

$$\tau_{1p} = B_{1p}(q_{1p})\ddot{x}_{1p}/r_1 + g_{1p}(q_{1p}) + \tau_f^{1p} + J_{1p}^{T}F_{ext}^{1p} \tag{13}$$

where:

$$\begin{cases} \tau_{1p} = \left(T_{1p} - T_{2p} - F_{f1p} - F_{f2p}\right) r_1 \\ B_{1p}(q_{1p}) = m_1 l_{g1}^2 + m_{2c}a_1^2 + m_{2c}l_{g2c}^2\cos^2(\theta_{2c}) \\ g_{1p}(q_{1p}) = -m_1 g l_{g1}\cos(\theta_{1p}) + m_{2c}g a_1 \sin(\theta_{1p}) \\ \qquad + m_{2c}g l_{g2c}\sin(\theta_{1p})\cos(\theta_{2c}) \\ J_{1p}^{T} = -a_1 - a_2\cos(\theta_{2x}), \quad F_{ext}^{1p} = F_{ext}^{z} \end{cases} \tag{14}$$

Combining (13) and (14) yields:

$$T_{1p} - T_{2p} - F_f^{1p} = B_{1p}(q_{1p})\ddot{x}_{1p}/r_1 \tag{15}$$

where: $F_f^{1p} = F_{f1p} + F_{f2p} + \tau_f^{1p}/r_1 + g_{1p}(q_{1p}) + J_{1p}^{T}F_{ext}^{1p}$.

When the pitch joint moves freely ($F_{ext}^{1p} = 0$), the comprehensive resistance model of the pitch joint is as follows:

$$\begin{aligned} F_{fmr}^{1p} &= T_{mr1p} - T_{mr2p} - B_{1p}(q_{1p})\ddot{x}_{1p}/r_1 \\ &= F_{fmr1p} + F_{fmr2p} + \tau_{fmr}^{1p}/r_1 + g_{1p}(q_{1p}) \end{aligned} \tag{16}$$

where T_{mr1p}, T_{mr2p}, F_{fmr1p}, F_{fmr2p}, τ_{fmr}^{1p} are the traction cable tension, reset cable tension, traction loop friction, reset loop friction, and joint friction torque, respectively.

B. COMPREHENSIVE RESISTANCE MODELING OF DEFLECTION JOINT

The driving force acts on the deflection joint in a similar manner to that described in Section 3.1. When the pitch joint is locked (pitch joint angle $\theta_{1p} = x_{1p}/r_1$ is a constant), the following relationship holds:

$$\begin{bmatrix} \dot{q}_{1p} \\ \dot{q}_{2x} \end{bmatrix} = \begin{bmatrix} \dot{\theta}_{1p} \\ \dot{\theta}_{2x} \end{bmatrix} = \begin{bmatrix} 0 \\ \dot{x}_{2x}/r_2 \end{bmatrix}, \begin{bmatrix} \ddot{q}_{1p} \\ \ddot{q}_{2x} \end{bmatrix} = \begin{bmatrix} \ddot{\theta}_{1p} \\ \ddot{\theta}_{2c} \end{bmatrix} = \begin{bmatrix} 0 \\ \ddot{x}_{2x}/r_2 \end{bmatrix} \tag{17}$$

Combining (7), (11) and (17) yields the following dynamic model of integrated deflection joint:

$$\tau_{2c} = B_{2c}(q_{2c})\ddot{x}_{2c}/r_2 + g_{2c}(q_{2c}) + \tau_f^{2c} + J_{2c}^{T}F_{ext}^{2c} \tag{18}$$

where:

$$\begin{cases} \tau_{2c} = (T_{1c} - T_{2c} - F_{f1c} - F_{f2c})\, r_2 \\ T_{1c} = T_{1a} + T_{1b}, T_{2c} = T_{2a} + T_{2b} \\ F_{f1c} = F_{f1a} + F_{f2a}, \quad F_{f2c} = F_{f1b} + F_{f2b} \\ B_{2c}(q_{2c}) = m_2 l_{g2}^2 \\ g_{2c}(q_{2c}) = m_2 g l_{g2}\cos(\theta_{1p})\sin(x_{2c}/r_2) \\ J_{2c}^{T} = a_2, F_{ext}^{2c} = F_{ext}^{y} \end{cases} \tag{19}$$

Combining (18) and (19) yields:

$$(T_{1a}+T_{1b})-(T_{2a}+T_{2b})-F_{f}^{2c}=B_{2c}(q_{2c})\ddot{x}_{2c}/r_2 \quad (20)$$

where $F_{f}^{2c}=F_{f1c}+F_{f2c}+\tau_{f}^{2c}/r_2+g_2(q_{2c})+J_{2c}^{T}F_{ext}^{2c}$.

If the pitch moves freely ($F_{ext}^{2c}=0$), the comprehensive resistance model of the deflection joint is:

$$\begin{aligned}F_{fmr}^{2c}&=(T_{mr1a}+T_{mr1b})-(T_{mr2a}+T_{mr2b})-B_{2c}(q_{2c})\ddot{x}_{2c}/r_2\\&=F_{fmr1c}+F_{fmr2c}+\tau_{fmr}^{2c}/r_2+g_2(q_{2c})\end{aligned} \quad (21)$$

where T_{mr1a}, T_{mr2a} are the traction cable tension and reset cable tension of joint A, T_{mr1b}, T_{mr2b} are the traction cable tension and reset cable tension of joint B, and F_{fmr1c}, F_{fmr2c}, τ_{fmr}^{1c} are the traction loop friction, reset loop friction, and joint friction torque of the integral deflection joint, respectively.

Combining Eq. 7, Eq. 12, and Eq. 17 yields dynamic model of deflection joint A:

$$\tau_{2a}=B_{2a}(q_{2a})\ddot{x}_{2a}/r_2+g_{2a}(q_{2a})+\tau_{f}^{2a}+J_{2a}^{T}F_{ext}^{2a} \quad (22)$$

where:

$$\begin{cases}\tau_{2a}=(T_{1a}-T_{2a}-F_{f1a}-F_{f2a})\,r_2\\B_{2a}(q_{2a})=m_2l_{g2a}^2\\g_{2a}(q_{2a})=m_{2a}gl_{g2a}\cos(\theta_{1p})\sin(x_{2a}/r_2)\\J_{2a}^{T}=a_2,\quad F_{ext}^{2a}=F_{ext}^{y}\end{cases} \quad (23)$$

Combining (22) and (23) yields the following:

$$T_{1a}-T_{2a}-F_{f}^{2a}=B_{2a}(q_{2a})\ddot{x}_{2a}/r_2 \quad (24)$$

where $F_{f}^{2a}=F_{f1a}+F_{f2a}+\tau_{f}^{2a}/r_2+g_{2a}(q_{2a})+J_{2a}^{T}F_{ext}^{2a}$.

If the deflection joint A moves freely ($F_{ext}^{2a}=0$), the comprehensive resistance model of the deflection joint A is:

$$\begin{aligned}F_{fmr}^{2a}&=T_{mr1a}-T_{mr2a}-B_{2a}(q_{2a})\ddot{x}_{2a}/r_2\\&=F_{fmr1a}+F_{fmr2a}+\tau_{fmr}^{2a}/r_2+g_2(q_{2a})\end{aligned} \quad (25)$$

where T_{mr1a}, T_{mr2a}, F_{fmr1a}, F_{fmr2a}, τ_{fmr}^{1a} are the traction cable tension, reset cable tension, traction loop friction, reset loop friction, and joint friction torque of deflection joint A, respectively.

The comprehensive resistance modeling of the deflection joint B can be obtained similarly:

$$\begin{aligned}F_{fmr}^{2b}&=T_{mr1b}-T_{mr2b}-B_{2b}(q_{2b})\ddot{x}_{2b}/r_2\\&=F_{fmr1b}+F_{fmr2b}+\tau_{fmr}^{2b}/r_2+g_2(q_{2b})\end{aligned} \quad (26)$$

C. COMPREHENSIVE RESISTANCE ESTIMATION MODEL

As the accelerations of the joint angles and the mass of the forceps are small, so the influence of inertia force canbe neglected. The comprehensive resistance models of each joint drive unit are as follows

$$\begin{cases}F_{fmr}^{1p}=T_{mr1p}-T_{mr2p}=F_{fmr1p}+F_{fmr2p}+\tau_{fmr}^{1p}/r_1\\\qquad+g_{1p}(q_{1p})\\F_{fmr}^{2a}=T_{mr1a}-T_{mr2a}=F_{fmr1a}+F_{fmr2a}+\tau_{fmr}^{2a}/r_2\\\qquad+g_2(q_{2a})\\F_{fmr}^{2b}=T_{mr1b}-T_{mr2b}=F_{fmr1b}+F_{fmr2b}+\tau_{fmr}^{2b}/r_2\\\qquad+g_2(q_{2b})\end{cases} \quad (27)$$

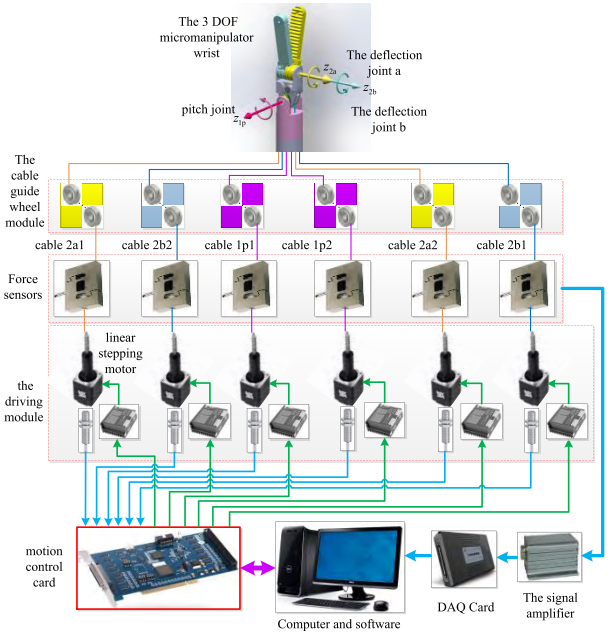

FIGURE 4. System composition block diagram of micromanipulator.

There is no element to detect the joint angle and cable displacement. The only information which can be obtained in the system includes the displacement, speed of the stepper motor, and tension of the cables. The parameters in (27) cannot be determined. Because the BP neural network has excellent performance in nonlinear function fitting and estimation, comprehensive resistance can be determined by training the neural network when the joint moves freely. With the displacement and speed of the stepper motor regarded as the input and the difference value between cable tensions as the output, we used the MATLAB neural network toolbox to complete the BP neural network training [26]. The trained neural network model $f_{BP}(x,\dot{x})$ is shown in (28), and it is the resistance neural network model of each joint. The training results are discussed in detail in Section 4.

$$\begin{cases}\hat{F}_{fmr}^{1p}=f_{BP}^{1p}(x_{1p},\dot{x}_{1p})=T_{mr1p}-T_{mr2p}\\\hat{F}_{fmr}^{2a}=f_{BP}^{2a}(x_{2a},\dot{x}_{2a})=T_{mr1a}-T_{mr2a}\\\hat{F}_{fmr}^{2b}=f_{BP}^{2b}(x_{2b},\dot{x}_{2b})=T_{mr1b}-T_{mr2b}\end{cases} \quad (28)$$

IV. COMPREHENSIVE RESISTANCE ESTIMATION EXPERIMENT

In order to study the influence of the touch force and clamping force to cable tension. The experimental system prototype of force sensing for the micromanipulator was set up, as is shown in Fig. 5. A system composition block diagram of the micromanipulator is shown in Fig. 4 highlighting the 3 -DOF wrist mechanism, cable guide wheel module, cable tension detection module, traction and reset module, PC control system, and operating software. The wrist's maximum overall diameter is 8 mm. Further descriptions of the system components are provided in Table 2.

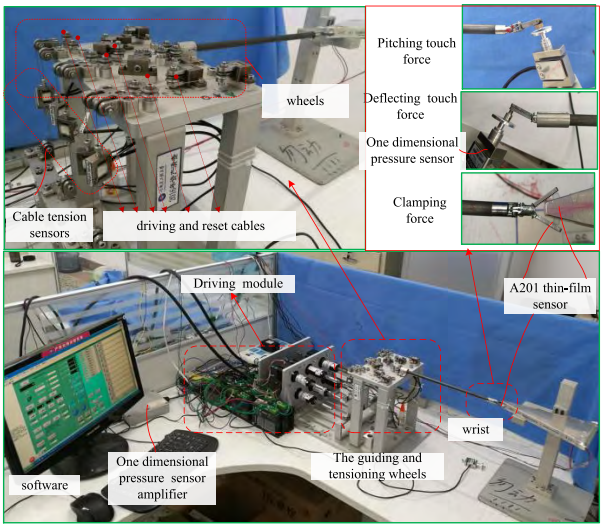

FIGURE 5. Experimental system prototype of force-sensing for micromanipulator.

TABLE 2. System components.

Component	Model	Parameter	Manufacturer
Cable	CG719045	R=0.45mm	Carl Stahl TECHNOCABLES
Force sensor/signal amplifier	EVT-10G-5kg/ EVT-1100A	0-50N	Shanghai Youran
Linear stepping motor/actuator	57H43-05-077/ DCM5040	0.00127mm /pulse	Haidun
DAQ card	USB5935	12-bit resolution	Artai
Motion control card	DMC2610	6 axis	Leisai

We used an MAB force sensor (type: Japan TRSB, range: -10 N-10 N) and amplifier (type: MAT528) to detect the deflection and pitch joint external forces. We also used American Tekscan FlexiForceA201 flexible pressure sensors to detect clamping force, as shown in Fig. 5. Our goal was to determine the force acting on the operating forceps during touch and clamp operations, as these would be the most important force information to be detected during an actual operation.

Prediction accuracy can be ensured if the displacement and speed of the stepper motor velocity belong to the training sample. Otherwise, there is no guarantee of prediction accuracy or stability, which is the primary limitation of this method. Extending the motor speed range of the experiment could have improved the prediction ability of the model. When the joints move freely, we used the MATLAB neural network toolbox to complete the BP neural network training. The network topology is 3 layers, input layer, single hidden layer and the output layer. The neurons number of input layer is 2, the input data are drive motor displacement and speed. The neurons number of single hidden layer is 100. The neurons number of output layer is 1, the output data is driven cable tension difference. The data normalization is the maximum and minimum methods. Node transfer function is "tansig", Training function is Levenberg-Marquard, and learning rules is Gradient Descent with Momentum. Performance analysis function is Mean Square Error. The sample data is 8000 points, the 80% of the data were used for training and 20% were used for verification.

Pitch joint comprehensive resistance BP neural network fitting results show that the mean absolute error is 0.1681 N and the root mean square error is 0.0711 N. the estimation precision is about 98.3%. When deflection joints A and B move freely (with pitch locked), the deflection joint comprehensive resistance BP neural network fitting results show that the mean absolute errors are 0.1788 N and 0.1910 N and root mean square errors are 0.2290 N and 0.2447 N. the precision are 96.8% and 97.5%. When the pitch joint is at the initial position, the deflection joints A and B complete the open-close operation; deflection joints comprehensive resistance BP neural network fitting results show mean absolute errors of 0.0613 N and 0.0615 N, with root mean square errors of 0.0014 N and 0.0013 N. the precision are 96.8% and 98.5%. (These results are not shown below due to space limitations.) The precision of the BP neural network fitting results is altogether satisfactory.

V. 2D TOUCH FORCE AND CLAMPING FORCE DETECTION EXPERIMENT

According to the joint characteristics of the micromanipulator loading experiment system, when detecting touch force, both operating forceps A and B must be regarded as a whole. The wrist in this case has two DOF and the 2D external force $\left[\hat{F}^{y}_{\text{ext}}\ \hat{F}^{z}_{\text{ext}}\right]^{T}$ can be detected. When the micromanipulator completes the clamping operation, the clamping force is perpendicular to the link. The two deflection joints can detect the operating forceps' external forces $\hat{F}^{y}_{\text{ext2a}}$ and $\hat{F}^{y}_{\text{ext2b}}$, respectively. The 2D touch force and the clamping force are expressed as follows:

$$\begin{cases} \hat{F}^{yz}_{\text{ext}} = \left[\hat{F}^{y}_{\text{ext}}\ \hat{F}^{z}_{\text{ext}}\right]^{\text{T}} \\ \hat{F}_{\text{C}} = \left(\left|\hat{F}^{y_a}_{\text{ext}}\right| + \left|\hat{F}^{y_b}_{\text{ext}}\right|\right)/2 \end{cases} \tag{29}$$

Combining (7), (8), (16), (21), (25), (26), and (29) yields the following estimation formula of the 2D touch force and clamping force:

$$\begin{cases} \hat{F}^{y}_{\text{ext}} = \hat{F}^{y_a}_{\text{ext}} + \hat{F}^{y_b}_{\text{ext}} \\ \hat{F}^{z}_{\text{ext}} = \left(J^{\text{T}}_{1\text{p}}\right)^{-1}\left[T_{1\text{p}} - T_{2\text{p}} - \hat{F}^{1\text{p}}_{\text{fmr}} - g_{1\text{p}}(q_{1\text{p}})\right] r_1 \\ \hat{F}^{y_a}_{\text{ext}} = \left(J^{\text{T}}_{2\text{a}}\right)^{-1}\left[T_{1\text{a}} - T_{2\text{a}} - \hat{F}^{2\text{a}}_{\text{fmr}} - g_{2\text{a}}(q_{2\text{a}})\right] r_2 \\ \hat{F}^{y_b}_{\text{ext}} = \left(J^{\text{T}}_{2\text{b}}\right)^{-1}\left[T_{1\text{b}} - T_{2\text{b}} - \hat{F}^{2\text{b}}_{\text{fmr}} - g_{2\text{b}}(q_{2\text{b}})\right] r_2 \end{cases} \tag{30}$$

The traction cable tension detection value and reset cable tension detection value of the pitch joint and deflection joints A and B are $T_{1\text{p}}$, $T_{2\text{p}}$, $T_{1\text{a}}$, $T_{2\text{a}}$, $T_{1\text{b}}$, $T_{2\text{b}}$, respectively. Comprehensive resistance BP neural network models of each joint

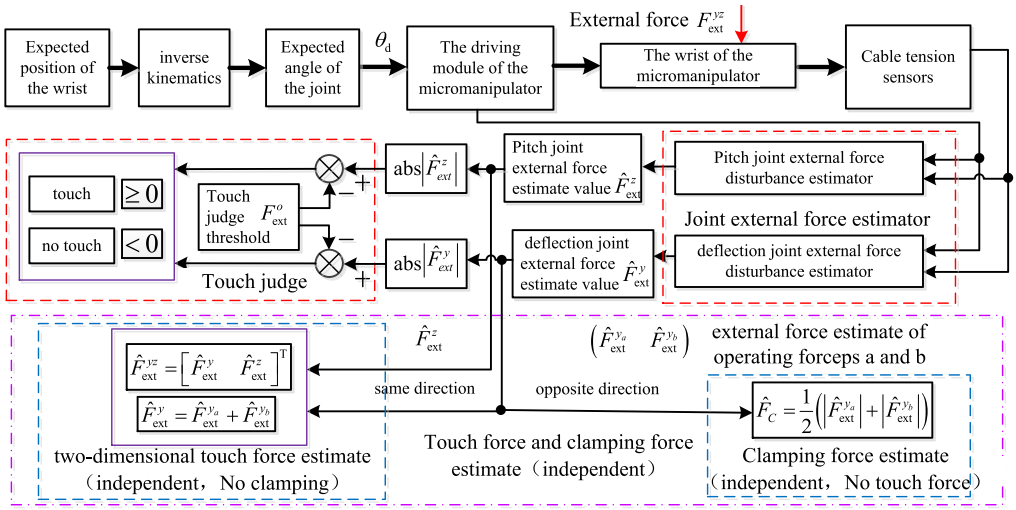

FIGURE 6. Block diagram of touch detection and estimation strategy of external force.

(no external force) are shown in (28), and Jacobian force is expressed as (31). Gravity compensation is shown in (32).

$$\begin{bmatrix} J_{1p}^{T} & J_{2a}^{T} & J_{2b}^{T} \end{bmatrix} = \begin{bmatrix} -a_1 - a_2\cos(\theta_{2x}) & a_2 & a_2 \end{bmatrix} \tag{31}$$

$$\begin{cases} g_{1p}(q_{1p}) = -m_1 g l_{g1}\cos(\theta_{1p}) + m_{2c} g a_1 \sin(\theta_{1p}) \\ \qquad\qquad + m_{2c} g l_{g2c}\sin(\theta_{1p})\cos(\theta_{2c}) \\ g_{2a}(q_{2a}) = m_{2a} g l_{g2a}\cos(\theta_{1p})\sin(\theta_{2a}) \\ g_{2b}(q_{2b}) = m_{2b} g l_{g2b}\cos(\theta_{1p})\sin(\theta_{2b}) \end{cases} \tag{32}$$

A. EXTERNAL FORCE TOUCH DETECTION STRATEGY

The contact force detection of the micromanipulator can be divided into three stages.

1) Free movement (no external force acts on the end).

2) Touching moment (transient process between free movement and the contact state).

3) Contact state (external force acts on the end).

The touch detection value is the sensitivity of the external force estimator (i.e., minimum resolution). The touch detection estimation strategy is shown in Fig. 6. The cable tension values change as the micromanipulator moves to the desired position and contacts the outside environment. The external force disturbance estimator of the pitch joint and deflection joint A and B were designed based on (29)-(32). The estimation values are $\hat{F}_{ext}^{z}$, $\hat{F}_{ext}^{y_a}$ and $\hat{F}_{ext}^{y_b}$. If one or more estimation value is larger than the "touch judge threshold" F_{ext}^{o}, the touch status can be determined; otherwise, no touch has occurred.

Limitations in our experimental system's machining precision rendered us incapable of ensuring joint linkage precision that meets the coupling analysis requirements for touch force and clamping force. The 2D touch force and clamping force were researched independently to explore a novel micromanipulator force detection technique. As shown in Fig. 6, if $\hat{F}_{ext}^{y_a}$ and $\hat{F}_{ext}^{y_b}$ have the same direction, the 2D touch force estimation value is $\hat{F}_{ext}^{yz}$. If $\hat{F}_{ext}^{y_a}$ and $\hat{F}_{ext}^{y_b}$ have the opposite direction, the clamping force estimation value is $\hat{F}_C$. The external force detection for the pitch joint and deflection joints are discussed in Section*5.B;* the clamping force detection is discussed in Section *5.C.*

B. 2D TOUCH FORCE ESTIMATION STRATEGY AND EXPERIMENT

Limited funds and mechanism precision left us without a multidimensional force sensor for the purposes of this study. We used a one-dimensional force sensor for direct force detection only. The 2D touch force can be separated into pitch joint external force $\hat{F}_{ext}^{z}$ and deflection joint external force $\hat{F}_{ext}^{y}$.

1) PITCH JOINT FORCE ESTIMATION STRATEGY AND EXPERIMENT

We established the pitch joint external force $\hat{F}_{ext}^{z}$ estimation strategy as shown in Fig. 7. We conducted loading and estimation at different pitch and deflection angles $[\theta_{1p}\theta_{2c}]$. The experimental results of the positive-direction loading process were shown in Figs. 8 and 9, where the collision detection threshold was $F_{ext}^{o} = 0.15$N.

The experiment was conducted in the following steps.

1) The pitch joint was placed at the initial "static" position (-60 deg).

2) The pitch joint began to move at the "starting instant".

3) The pitch moved from the initial to the expected position during the "loading process".

4) "Collision detection" occurred at the moment the operating forceps contacted the sensor.

5) The system reached the "stability region" once pitch joint movement ceased.

Six groups of different pitch and deflection angles $[\theta_{1p}\theta_{2c}]$ were set to complete the estimation experiment. Different situations (L,O,R), as shown in Fig. 8 and Fig. 9, involved the

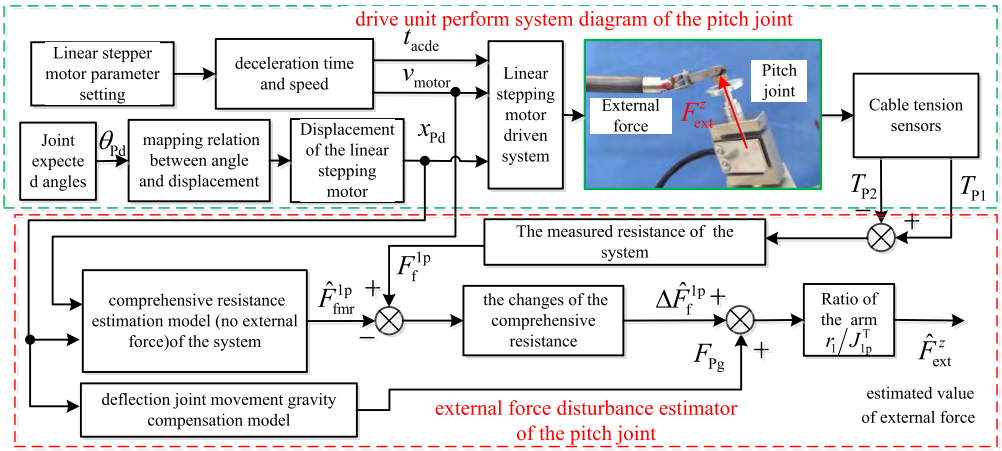

FIGURE 7. Block diagram of external force estimation strategy of pitch joint.

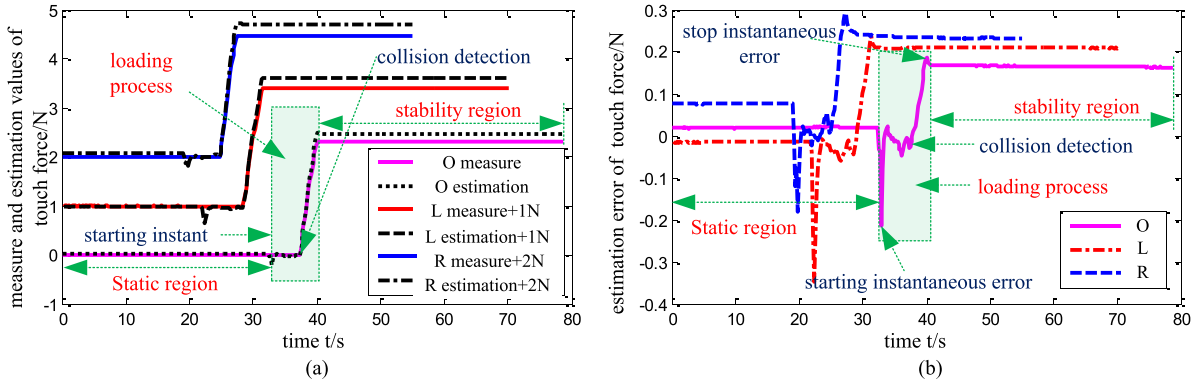

(note: O: $[\theta_{1p}\ \theta_{2c}]$ = [0 0] deg L : $[\theta_{1p}\ \theta_{2c}]$ = [0 -30.13] deg; R: $[\theta_{1p}\ \theta_{2c}]$ = [0 39.70] deg)

FIGURE 8. Experimental results (1) of continuous positive external force estimation of pitch joint. (a) measure and estimation values of touch force. (b) estimation error of touch force.

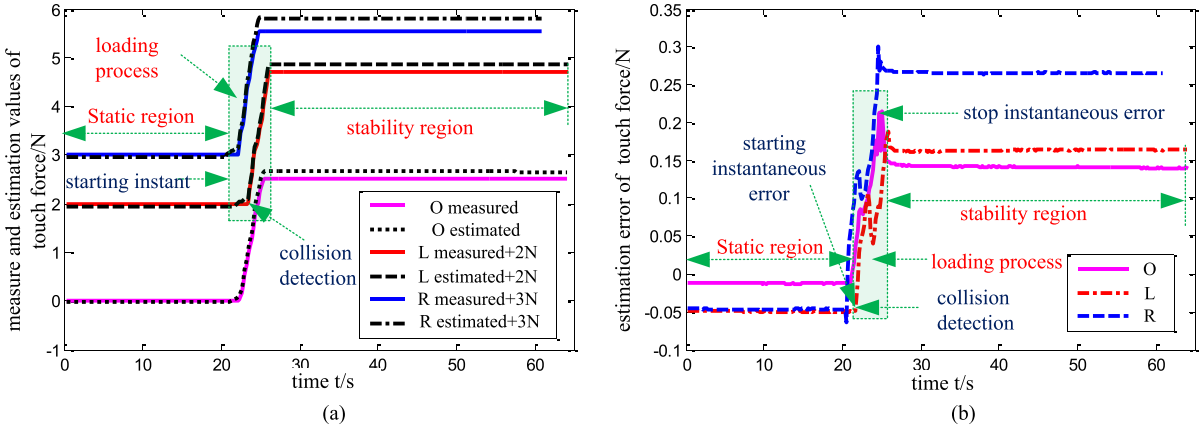

(note: O: $[\theta_{1p}\ \theta_{2c}]$ =[-19.76 0] deg; L: $[\theta_{1p}\ \theta_{2c}]$ = [-23.59 -30.13] deg; R: $[\theta_{1p}\ \theta_{2c}]$ = [-23.59 39.70] deg)

FIGURE 9. Experimental results (2) of continuous positive external force estimation of pitch joint. (a) measure and estimation values of touch force. (b) estimation error of touch force.

pitch joint moving from −60 deg to θ_{1p} as a positive external force was loaded on the joint. Sub-figure (a) described the measured values and the estimated values of three different situations; Sub-figure (b) described the estimated errors. There was a larger transient estimation error at the "start" and "stop" moments of the experiment.

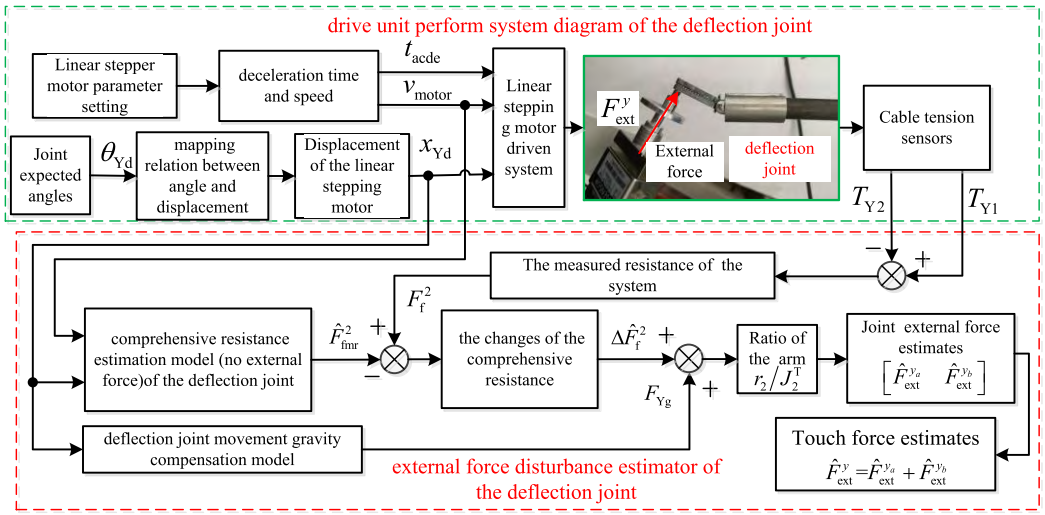

FIGURE 10. Block diagram of external force estimation strategy of deflection joint.

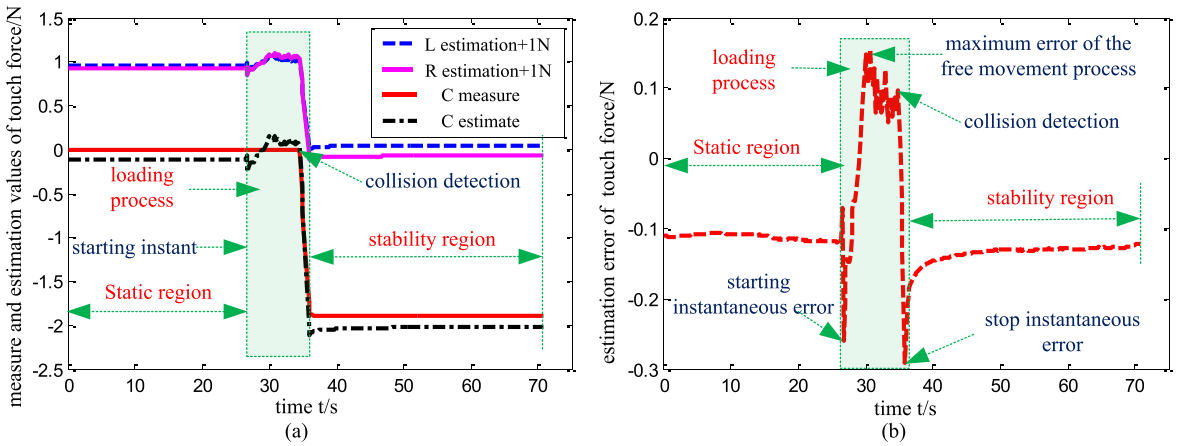

FIGURE 11. Experimental results (1) of continuous negative external force estimation of deflection joints. (a) Measure and estimation values of touch force. (b) Estimation error of touch force.

We plotted experimental curves along the corresponding coordinate system to make these results more clearly observable. Transient error did not affect the steady-state force estimation performance, and the estimation error range was ±0.3 N among the experimental processes. The estimation precision $[P_O, P_L, P_R]$ of the "stability region" were [92.79%, 91.12%, 90.04%] and [94.13%, 93.76%, 89.38%], respectively.

Next, negative-direction external force was loaded on the pitch joint as it moved from 60 deg to θ_{1p}. The same experiments were run again under these conditions to obtain estimation precisions $[P_O, P_L, P_R]$ of the "stability region" [97.79%, 88.55%, 88.55%] and [96.42%, 96.91%, 96.38%]. The average estimation precision of the steady state was 92.69%. The absolute error of the estimation value of $\hat{F}^z_{ext}$ was about -0.17 N in the stability region. In other words, the steady-state estimation precision of $\hat{F}^z_{ext}$ was trustworthy. The minimum resolutionF^o_{ext} was 0.15N.

2) DEFLECTION JOINT FORCE ESTIMATION STRATEGY AND EXPERIMENT

The deflection joint external force $\hat{F}^y_{ext}$ estimation strategy was established as is shown in Fig. 10. We loaded and estimated pitch angle $\theta_{1p} = 0$ and different θ_{2c} to obtain the experiment results of the negative-direction loading process shown in Figs. 11 and 12. As an external force was applied on joint B, the collision detection threshold was $F^o_{ext} = 0.15$N. In the figures, "L estimation" is the estimated value of joint B external force and "R estimation" is the estimated value of joint A external force. "C measure" and "C estimation" are the measured and estimated values of the integrated deflection joints. The estimation errors were shown in Figs. 11(b) and 12(b).

The experimental process is similar to the pitch joint force estimation process, (a) descried the measure values and the estimation values, (b) descried the estimation errors. There was a larger transient estimation error at the start and stop

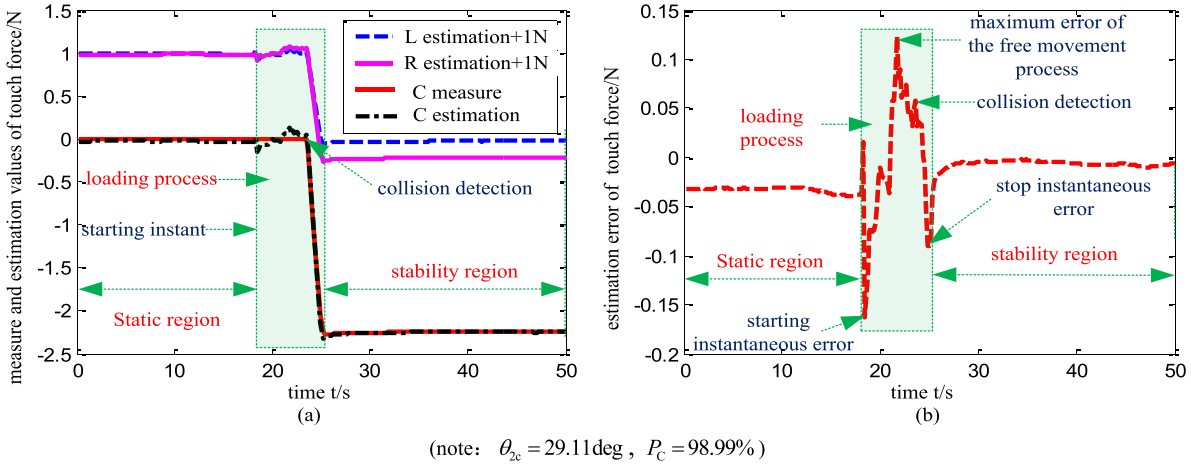

(note: $\theta_{2c} = 29.11\text{deg}$, $P_C = 98.99\%$)

FIGURE 12. Experimental results (3) of continuous negative external force estimation of deflection joints. (a) Measure and estimation values of touch force. (b) Estimation error of touch force.

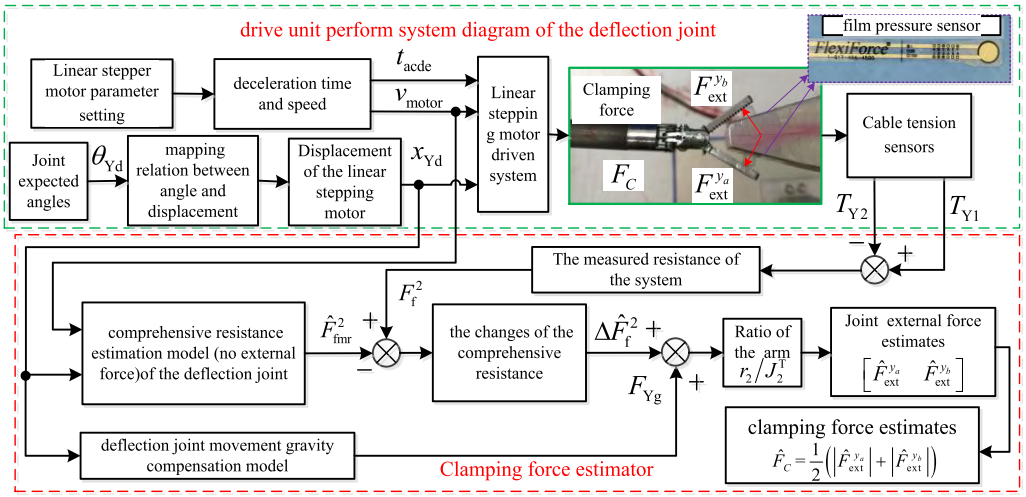

FIGURE 13. Block diagram of clamping force estimation strategy of the micromanipulator.

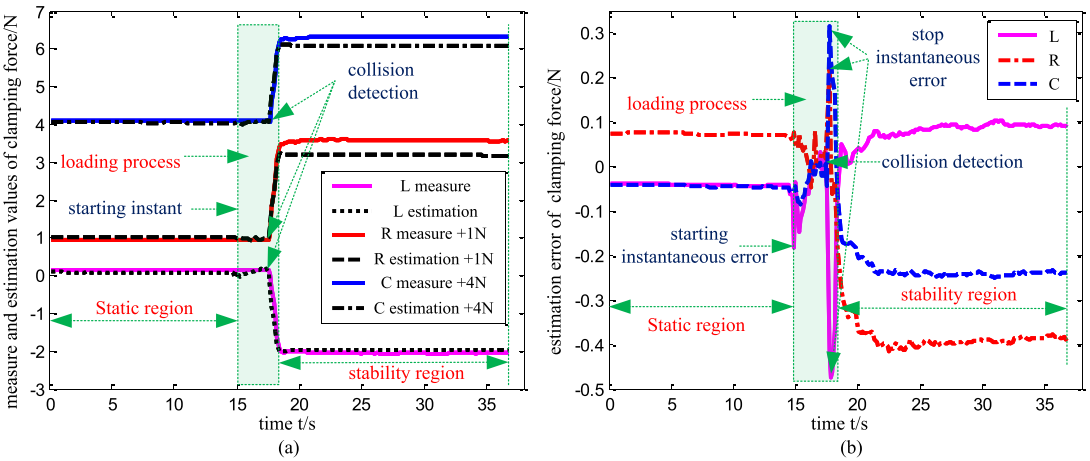

FIGURE 14. Experimental results of continuous clamping force estimation. (a) measure and estimation values of clamping force. (b) estimation error of clamping force.

moment. The transient error does not affect the steady-state force estimation performance. The estimation error range was −0.28 N to 0.15 N throughout our experimental process and the mean estimation precision P_C was 95.95%. The absolute error of the deflection joint external force $\hat{F}_{ext}^{y}$ estimation value $\hat{F}_{ext}^{y}$ was about −0.1N in the stability region. In the

position direction loading experiment, when the external force acted on the deflection joint A, the mean estimation precision was 93.88%. These results altogether indicated that the steady-state estimation precision of $\hat{F}_{\text{ext}}^{y}$ was trustworthy.

C. CLAMPING FORCE ESTIMATION STRATEGY AND EXPERIMENT

The clamping force estimation strategy was established as is shown in Fig. 13. The range of the film pressure sensors in this experiment was 0-4 N.

The two operating forceps A and B touched the sensors when the opening angle of the wrist was 65 deg. The experimental results of continuous clamping force estimation were shown in Fig. 14. The clamping force threshold value was $F_{\text{ext}}^{o} = 0.10\text{N}$, where "L measure" and "L estimation" are the measured and estimated value of operating forceps A's external force; "R measure" and "R estimation" are the measured and estimated values of operating forceps B's external force; "C measure" and "C estimation" are the measured and estimated values of clamping force. The estimation error of the continuous clamping force estimation ranged from −0.24 N to 0.3 N. The estimation precision of external force $\hat{F}_{\text{ext}}^{y_a}$ and $\hat{F}_{\text{ext}}^{y_b}$ was 94.51% and 84.20%, and the estimation precision of clamping force $\hat{F}_C$ was 89.35%. The absolute error of the clamping force $\hat{F}_C$ was about −0.24 N in the stability region. These results indicated that the proposed clamping force estimation method is highly accurate.

VI. CONCLUSION

This paper proposed an indirect 2D touch and clamping force detection method based on changes in driving cable tension for surgical robot micromanipulators. We first established the complete dynamic model and an external force estimation strategy based on comprehensive changes in the driving system, then conducted a resistance experiment in a prototype pitch joint and two deflection joints as the system moved freely. We obtained the corresponding resistance model via BP neural network nonlinear fitting. We then tested the proposed external force and clamping force estimation method experimentally. The results show that the estimation precision is acceptable. And the proposed method has a higher precision compared with the other indirect detection methods.

REFERENCES

[1] T. Haidegger and Z. Benyo, "Surgical robotic support for long duration space missions," *Acta Astron.*, vol. 63, nos. 7–10, pp. 996–1005, 2008.
[2] N. Monsarrat *et al.*, "Robotic assistance in gynaecological surgery: State-of-the-art," *Gynecologie, Obstetrique Fertilite*, vol. 37, no. 5, pp. 415–424, 2009.
[3] M. Kitagawa, D. Dokko, A. M. Okamura, and D. D. Yuh, "Effect of sensory substitution on suture-manipulation forces for robotic surgical systems," *J. Thoracic Cardiovascular Surgery*, vol. 129, no. 1, pp. 151–158, Jan. 2005.
[4] G. Tholey, J. P. Desai, and A. E. Castellanos, "Force feedback plays a significant role in minimally invasive surgery: Results and analysis," *Ann. Surgery*, vol. 241, no. 1, pp. 102–109, 2005.
[5] B. Zhao and C. A. Nelson, "Estimating tool–tissue forces using a 3-degree-of-freedom robotic surgical tool," *J. Mech. Robot.*, vol. 8, no. 5, p. 051015, 2016.
[6] F. Yili, K. Li, B. Pan, J. Zhan, and S. Wang, "A survey of force sensing and force feedback technology for robot-assisted minimally invasive surgical system," *Robot*, vol. 36, no. 1, pp. 117–128.
[7] J. D. Brown, J. Rosen, M. Moreyra, M. Sinanan, and B. Hannaford, "Computer-controlled motorized endoscopic grasper for *in vivo* measurement of soft tissue biomechanical characteristics," in *Stud. Health Technol. Inform.*, vol. 85, pp. 71–73, 2001.
[8] S. K. Prasad *et al.*, "A modular 2-DOF force-sensing instrument for laparoscopic surgery," in *Medical Image Computing and Computer-Assisted Intervention—MICCAI*. Berlin, Germany: Springer, 2003, pp. 279–286, doi: 10.1007/978-3-540-39899-8_35.
[9] A. Menciassi, A. Eisinberg, M. C. Carrozza, and P. Dario, "Force sensing microinstrument for measuring tissue properties and pulse in microsurgery," *IEEE/ASME Trans. Mechatronics*, vol. 8, no. 1, pp. 10–17, Mar. 2003.
[10] J. B. Gafford, S. B. Kesner, R. J. Wood, and C. J. Walsh, "Force-sensing surgical grasper enabled by pop-up book MEMS," in *Proc. IEEE/RSJ Int. Conf. Intell. Robots Syst. (IROS)*, Tokyo, Japan, 2013, pp. 2552–2558.
[11] B. Kübler, U. Seibold, and G. Hirzinger, "Development of actuated and sensor integrated forceps for minimally invasive robotic surger," *Int. J. Med. Robot. Comput. Assist. Surgery*, vol. 1, no. 3, pp. 96–107, 2005.
[12] F. L. Hammond, M. J. Smith, and R. J. Wood, "Printing strain gauges on surgical instruments for force measurement," *J. Med. Devices*, vol. 8, no. 3, p. 030935, 2014.
[13] J. Peirs *et al.*, "A micro optical force sensor for force feedback during minimally invasive robotic surgery," *Sens. Actuators A, Phys.*, vol. 115, nos. 2–3, pp. 447–455, 2004.
[14] P. Puangmali, H. Liu, L. D. Seneviratne, P. Dasgupta, and K. Althoefer, "Miniature 3-axis distal force sensor for minimally invasive surgical palpation," *IEEE/ASME Trans. Mechatronics*, vol. 17, no. 4, pp. 646–656, Aug. 2012.
[15] S.-C. Lim, H.-K. Lee, and J. Park, "Grip force measurement of forceps with fibre Bragg grating sensors," *Electron. Lett.*, vol. 50, no. 10, pp. 733–735, 2014.
[16] H. Xie, H. Liu, Y. Noh, J. Li, S. Wang, and K. Althoefer, "A fiber-optics-based body contact sensor for a flexible manipulator," *IEEE Sensors J.*, vol. 15, no. 6, pp. 3543–3550, Jun. 2015.
[17] P. Valdastri *et al.*, "Integration of a miniaturised triaxial force sensor in a minimally invasive surgical tool," *IEEE Trans. Biomed. Eng.*, vol. 53, no. 11, pp. 2397–2400, Nov. 2006.
[18] B. L. Gray and R. S. Fearing, "A surface micromachined microtactile sensor array," in *Proc. IEEE Int. Conf. Robot. Autom.*, vol. 1. Minneapolis, MN, USA, Apr. 1996, pp. 1–6.
[19] J. Rosen, B. Hannaford, M.-P. MacFarlane, and M.-N. Sinanan, "Force controlled and teleoperated endoscopic grasper for minimally invasive surgery-experimental performance evaluation," *IEEE Trans. Biomed. Eng.*, vol. 46, no. 10, pp. 1212–1221, Oct. 1999.
[20] G. Tholey, A. Pillarisetti, W. Green, and J. P. Desai, "Design, development, and testing of an automated laparoscopic grasper with 3-D force measurement capability," in *Medical Simulation*. Berlin, Germany: Springer, 2004, pp. 38–48.
[21] B. Zhao and C. A. Nelson, "Sensorless force estimation for a three degrees-of-freedom motorized surgical grasper," *J. Med. Devices*, vol. 9, no. 3, p. 030929, 2015.
[22] H. Mayer, F. Gomez, D. Wierstra, I. Nagy, A. Knoll, and J. Schmidhuber, "A system for robotic heart surgery that learns to tie knots using recurrent neural networks," *Adv. Robot.*, vol. 22, nos. 13–14, pp. 1521–1537, 2008.
[23] H. Li, K. Kawashima, K. Tadano, S. Ganguly, and S. Nakano, "Achieving haptic perception in forceps' manipulator using pneumatic artificial muscle," *IEEE/ASME Trans. Mechatronics*, vol. 18, no. 1, pp. 74–85, Feb. 2013.
[24] J. Denavit and R. S. Hartenberg, "A kinematic notation for lower-pair mechanisms based on matrices," *Trans. ASME. J. Appl. Mech.*, vol. 77, no. 22, pp. 215–221, 1955.
[25] R. M. Murray, S. S. Sastry, and Z. Li, *A Mathematical Introduction to Robotic Manipulation*. Boca Raton, FL, USA: CRC Press, 1994.
[26] S. Haykin, *Neural Networks: A Comprehensive Foundation*. Englewood Cliffs, NJ, USA: Prentice-Hall, 1994, pp. 71–80.

LINGTAO YU received the B.S., M.S., and Ph.D. degrees from the College of Mechanical and Electrical Engineering, Harbin Institute of Technology, in 2000, 2002, and 2007, respectively. From 2014 to 2015, he was a Visiting Scholar with the National University of Singapore. He is currently an Associate Professor in mechanical engineering with the Harbin Engineering University. He has authored two books, over 40 articles, and over ten inventions. His research interests include parallel robot, surgical robot, mechatronics, and biomechanics.

WENJIE WANG was born in Baoji, China, in 1988. He received the B.S. degree in mechanical engineering from the College of Mechanical and Electrical Engineering, Harbin Engineering University, in 2012, where he is currently pursuing the Ph.D. degree in mechanical engineering. His current research interests include surgical robot, mechatronics, and parallel robot.

FENGFENG ZHANG received the B.S., M.S., and Ph.D. degrees from the School of Mechanical and Electrical Engineering, Harbin Institute of Technology, in 2001, 2003, and 2009, respectively. He is currently an Associate Professor with the School of Mechanical and Electrical Engineering, Soochow University. He has authored over 30 articles and over eight inventions. His research interests include surgical robot, virtual reality, and biomechanics.